

# Regional Precipitation Nowcasting Based on CycleGAN Extension

Jaeho Choi, Yura Kim, Kwang-Ho Kim, Sung-Hwa Jung, and Ikhyun Cho

Weather Radar Center, Korea Meteorological Administration

{jaehochoi2021, yrkim110, khkim777, shjung95}@korea.kr, ehcho@kma.go.kr

## Abstract

*Unusually, intensive heavy rain hit the central region of Korea on August 8, 2022. Many low-lying areas were submerged, so traffic and life were severely paralyzed. It was the critical damage caused by torrential rain for just a few hours. This event reminded us of the need for a more reliable regional precipitation nowcasting method. In this paper, we bring cycle-consistent adversarial networks (CycleGAN) into the time-series domain and extend it to propose a reliable model for regional precipitation nowcasting. The proposed model generates composite hybrid surface rainfall (HSR) data after 10 minutes from the present time. Also, the proposed model provides a reliable prediction of up to 2 hours with a gradual extension of the training time steps. Unlike the existing complex nowcasting methods, the proposed model does not use recurrent neural networks (RNNs) and secures temporal causality via sequential training in the cycle. Our precipitation nowcasting method outperforms convolutional long short-term memory (ConvLSTM) based on RNNs. Additionally, we demonstrate the superiority of our approach by qualitative and quantitative comparisons against MAPLE, the McGill algorithm for precipitation nowcasting by lagrangian extrapolation, one of the real quantitative precipitation forecast (QPF) models.*

## 1. Introduction

Rain has had a close influence on human lives since ancient times. Therefore, precipitation forecasting has always been a topic of human interest. There have been many attempts to predict precipitation from a meteorological point of view. Typically, the development of numerical weather prediction (NWP) models has been at the center of these attempts [52, 56]. The NWP models support good quantitative precipitation forecasting across a wide timeline. However, the NWP models cannot guarantee accuracy in the first few hours because they develop the convective-scale structures in the early stages of forecasting [50]. This limitation is called a spin-up problem. To solve this problem, the importance of nowcasting, which focuses on short-term forecast-

ing, has increased.

In meteorology, nowcasting generally refers to a model or forecasting that accurately predicts weather within about two hours from now. In particular, the precipitation nowcasting is generally based on weather radar observations. Although various quantitative precipitation forecast (QPF) models exist [12, 54], perfect precipitation nowcasting is always a challenge. With the great success of generative models such as generative adversarial networks (GANs) [15, 16], there are increasing attempts to use these for precipitation nowcasting. However, there are very few successful cases. This is because precipitation data contain diverse distributions that are very hard to learn. In-depth analysis and understanding of precipitation data through collaboration between artificial intelligence researchers and meteorologists must be required.

Inspired by cycle-consistent adversarial networks (CycleGAN) [58], we propose a novel precipitation nowcasting method. We train two generators and two discriminators in two complementary cycles. One generator learns mapping into one step future, and the other learns mapping into one step past. The two discriminators determine whether the mapping into the future and the past are appropriate, respectively. Here, we focus on a regional part of the mesoscale convective system. Therefore, the mapping from the distributions of current precipitation echoes to the distributions of future precipitation echoes and vice versa can be finitely modeled. Also, since the mapping is time-dependent, it should guarantee the temporal causality that does not reverse or stop. We remove the identity loss added in the original CycleGAN and add paired data and pixel loss concepts to create robust temporal causality. As a result, our trained future prediction generator outperforms the existing representative QPF model, the McGill algorithm for precipitation nowcasting by lagrangian extrapolation (MAPLE) [54], during a lead time of two hours. And it also outperforms convolutional long short-term memory (ConvLSTM) [48], a representative recurrent neural networks (RNNs) series model for precipitation nowcasting. More specifically, it outperforms MAPLE and ConvLSTM in the critical success index (CSI) [47], which is a qualitative metric, and the

peak signal-to-noise ratio (PSNR) and structural similarity index measure (SSIM) [55], which are quantitative metrics.

The remainder of this paper is structured as follows. Section 2 briefly reviews related work. Section 3 describes our proposed objective functions and network architectures. Section 4 demonstrates the superiority of our proposed method through evaluation and discusses its limitations. Finally, we conclude the paper in Section 5.

## 2. Related Work

**Generative Adversarial Networks.** GANs are one of the most innovative ideas that have succeeded in the field of artificial intelligence [15, 32]. GANs consist of two kinds of networks, which are called generator and discriminator. The goal of the generator is to learn the probability distribution that generated the training data [16]. In other words, the generator becomes possible to generate fake data that is difficult to discriminate from real data through the training process. The goal of the discriminator is to distinguish between real and fake data. During the training process, the quality of generated fake data is increased via the discriminator’s feedback.

**Least Squares Generative Adversarial Networks.** The key to the optimization of the regular GANs is to minimize the Jensen-Shannon divergence (JSD) between the model’s distribution and the data-generating process [15]. However, this approach causes weaknesses such as mode collapse and learning instability. Thus, there were attempts to improve the objective function of regular GANs. Instead of the minimum of JSD, Wasserstein GANs (WGANs) [1], which find the minimum value of earth mover’s distance (EMD), and its improved version with gradient penalty (GP), WGAN-GP appeared [17]. And least squares GANs (LSGANs) [36, 37], which find the minimum value of Pearson  $\chi^2$  divergence, also appeared. In particular, LSGANs are used in many GAN-based applications because of their simple implementation and good performance [7, 8, 28, 40, 60]. We adopt the adversarial losses of LSGANs as a part of our optimization functions because of their faster and more stable convergence rate.

**Cycle-Consistent Adversarial Networks.** The image-to-image translation is one of the popular topics in the deep learning area, and various studies have been made [11, 21, 22, 26, 33, 34, 43, 58]. In particular, techniques based on GANs become a golden key in the field of image-to-image translation because of their powerful ability to formulate and generate high-resolution images [57]. As a pioneer, Pix2Pix succeeded in paired image-to-image translation using conditional GANs [22]. Based on this, CycleGAN solved the unpaired image-to-image translation using cycle-consistency loss [58]. CycleGAN, which assumes the relationship between the two domains as a bijection, is shown good performance in various fields [23, 27, 31, 38, 43]. In

particular, the study of Kwon and Park [27], which predicts the next frame for video, was impressive. However, their proposed multi-input-single-output generator, which should maintain the input sequence of images, can not be considered to provide temporal causality via CycleGAN by itself. We adopt CycleGAN but apply cycle-consistency loss to obtain temporal causality by itself without forced input sequence. Because of this point, our method can make great results with a single-input-single-output generator.

**Precipitation Nowcasting via Deep Learning.** Accurate precipitation nowcasting is a long-standing challenge in meteorology because rain has a huge impact on human life. Various meteorological models for precipitation nowcasting were built [10, 13, 14, 29, 39, 44, 52, 54], but it is always a difficult problem for humans to accurately consider complex factors for natural phenomena. As the deep learning model has great success in various fields, several attempts are active to apply this to precipitation nowcasting. The ConvLSTM, which can make better predictions than the method based on the optical flow of consecutive radar maps, appeared in 2015 [48]. Following the success of ConvLSTM, various models for precipitation nowcasting based on RNNs emerged to capture temporal changes in radar echoes [2, 5, 6, 24, 35, 49]. In 2020, RainNet, which uses an encoder-decoder architecture such as U-Net, appeared [3]. After the birth of RainNet, many models for precipitation nowcasting used U-Net architecture [4, 18, 46, 53]. In recent years, ResNet-based models are in the spotlight [19]. Two representative models using residual blocks of ResNet, the deep generative model of rainfall (DGMR) and MetNet-2 showed successful results for several hours of precipitation forecasting [9, 45]. To obtain temporal causality, DGMR and MetNet-2 use the convolutional gated recurrent unit (ConvGRU) and ConvLSTM, respectively [51]. In other words, both models also depend on RNNs. We adopt residual blocks for performance, but not RNNs. Nevertheless, our proposed model guarantees great predictive results within the scope of nowcasting.

## 3. Proposed Method

As described in Figure 1, our training model for precipitation nowcasting consists of two cycles and uses composite hybrid surface rainfall (HSR) as data [42]. A total of four different networks are trained in two cycles.  $Generator_{forward}$  and  $Generator_{backward}$  learn the mapping from present to future and from future to present, respectively.  $Discriminator(t_{i+step})$  and  $Discriminator(t_i)$  evaluate the mapping accuracy of  $Generator_{forward}$  and  $Generator_{backward}$ , respectively.

For clarity, we briefly explain the notations used in the rest of the paper. A sample of data,  $HSR_i$ , used as input to

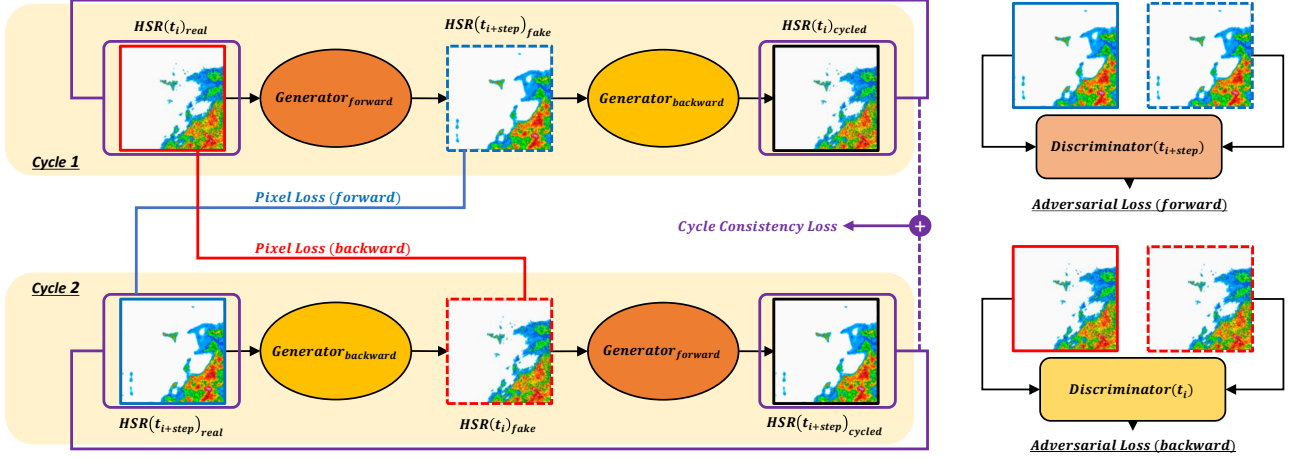


Figure 1. Training schematic of the proposed model for precipitation nowcasting. For the clear and concise explanation,  $Generator_{forward}$ ,  $Generator_{backward}$ ,  $Discriminator(t_{i+step})$ , and  $Discriminator(t_i)$  are denoted as  $G_f$ ,  $G_b$ ,  $D(t_{i+step})$ , and  $D(t_i)$ , respectively. Two generators ( $G_f$  and  $G_b$ ) and two discriminators ( $D(t_{i+step})$  and  $D(t_i)$ ) are trained via two cycles.  $G_f$  and  $G_b$  generate the fake composite hybrid surface rainfall (HSR) of the next time step and the previous time step from the input HSR, respectively.  $D(t_{i+step})$  discriminates the fake HSR generated by  $G_f$  and the real HSR. Similarly,  $D(t_i)$  discriminates the fake HSR generated by  $G_b$  and the real HSR. Cycle 1 generates the one-step fake future from the real  $HSR(t_i)$ , and generates cycled  $HSR(t_i)$  again from the generated future, i.e., Cycle 1  $\triangleq HSR(t_i)_{real} \rightarrow HSR(t_{i+step})_{fake} \rightarrow HSR(t_i)_{cycled}$ . Cycle 2 generates the one-step fake past from the real  $HSR(t_{i+step})$ , and generates cycled  $HSR(t_{i+step})$  again from the generated past, i.e., Cycle 2  $\triangleq HSR(t_{i+step})_{real} \rightarrow HSR(t_i)_{fake} \rightarrow HSR(t_{i+step})_{cycled}$ . The final goal of the model is to make real, fake, and cycled HSR identical. In other words, it should be  $HSR(t_i)_{real} \approx HSR(t_i)_{fake} \approx HSR(t_i)_{cycled}$  and  $HSR(t_{i+step})_{real} \approx HSR(t_{i+step})_{fake} \approx HSR(t_{i+step})_{cycled}$  after training.

the model is denoted as follows:

$$HSR_i \triangleq (HSR(t_i)_{real}, HSR(t_{i+step})_{real}), \quad (1)$$

where  $t_i$  is an arbitrary element of  $T_n = \{t_1, t_2, \dots, t_n\}$ , the arithmetic sequence of discrete-time;  $n \in \mathbb{Z}^+$ ,  $i \in \mathbb{Z}^+$ ,  $step \in \mathbb{Z}^+$ , and  $i + step \leq n$ . Note that  $HSR(t_i)_{real}$  represents real HSR data at time  $t_i$ . Cycle 1, which predicts the future from the known present and predicts the present again from the predicted future, is defined as follows:

$$\begin{aligned} \text{Cycle 1} &\triangleq HSR(t_i)_{real} \xrightarrow{G_f} HSR(t_{i+step})_{fake} \\ &\xrightarrow{G_b} HSR(t_i)_{cycled}, \end{aligned} \quad (2)$$

where subscripts *fake* and *cycled* represent data generated from *real* and data generated from *fake*, respectively;  $G_f$  and  $G_b$  indicate  $Generator_{forward}$  and  $Generator_{backward}$  in Figure 1, respectively. Cycle 2, which predicts the present from the known future and predicts the future again from the predicted present, is defined as follows:

$$\begin{aligned} \text{Cycle 2} &\triangleq HSR(t_{i+step})_{real} \xrightarrow{G_b} HSR(t_i)_{fake} \\ &\xrightarrow{G_f} HSR(t_{i+step})_{cycled}, \end{aligned} \quad (3)$$

where variables are identical to variables in Equation (2). In addition,  $Discriminator(t_{i+step})$  and  $Discriminator(t_i)$  are

denoted as  $D(t_{i+step})$  and  $D(t_i)$ , respectively. Therefore,  $\delta(t_{i+step})_{real}$ ,  $\delta(t_{i+step})_{fake}$ ,  $\delta(t_i)_{real}$ , and  $\delta(t_i)_{fake}$ , the outputs of  $D(t_{i+step})$  and  $D(t_i)$ , are denoted as follows:

$$\delta(t_{i+step})_{real} \triangleq D(t_{i+step})(HSR(t_{i+step})_{real}), \quad (4)$$

$$\delta(t_{i+step})_{fake} \triangleq D(t_{i+step})(HSR(t_{i+step})_{fake}), \quad (5)$$

$$\delta(t_i)_{real} \triangleq D(t_i)(HSR(t_i)_{real}), \quad (6)$$

$$\delta(t_i)_{fake} \triangleq D(t_i)(HSR(t_i)_{fake}). \quad (7)$$

And the  $L1$  norms  $L1(t_{i+step})_{fake}$ ,  $L1(t_{i+step})_{cycled}$ ,  $L1(t_i)_{fake}$ , and  $L1(t_i)_{cycled}$  are denoted as follows:

$$\begin{aligned} L1(t_{i+step})_{fake} &\triangleq \|HSR(t_{i+step})_{fake} - HSR(t_{i+step})_{real}\|_1, \end{aligned} \quad (8)$$

$$\begin{aligned} L1(t_{i+step})_{cycled} &\triangleq \|HSR(t_{i+step})_{cycled} - HSR(t_{i+step})_{real}\|_1, \end{aligned} \quad (9)$$

$$\begin{aligned} L1(t_i)_{fake} &\triangleq \|HSR(t_i)_{fake} - HSR(t_i)_{real}\|_1, \end{aligned} \quad (10)$$

$$\begin{aligned} L1(t_i)_{cycled} &\triangleq \|HSR(t_i)_{cycled} - HSR(t_i)_{real}\|_1. \end{aligned} \quad (11)$$

Note that Equations (4)–(7) are used in Section 3.1.1; Equations (8)–(11) are used in Section 3.1.2 and 3.1.3.

### 3.1. Optimization

Our proposed training model receives  $HSR_i$  as input and distributes  $HSR(t_i)_{real}$  and  $HSR(t_{i+step})_{real}$  to *Cycle 1* and *Cycle 2*, respectively. With the complementary optimization of *Cycle 1* and *Cycle 2*, the model obtains robust temporal causality. Our proposed objective functions can be formulated into three kinds of terms, *i.e.*, adversarial loss, cycle-consistency loss, and pixel loss. The description of the three losses continues in Section 3.1.1, 3.1.2, and 3.1.3, respectively.

#### 3.1.1 Adversarial Loss

We apply adversarial losses to match the distributions of  $HSR(t_{i+step})_{real}$  and  $HSR(t_{i+step})_{fake}$ . (*Adversarial Loss (forward)* in Figure 1.) Likewise, we also apply adversarial losses to match the distribution of  $HSR(t_i)_{real}$  and  $HSR(t_i)_{fake}$ . (*Adversarial Loss (backward)* in Figure 1.) In particular, we adopt the adversarial losses of LSGANs and extend them for two complementary cycles [36, 37]. In other words, our adversarial losses are as follows:

$$\begin{aligned} \mathcal{L}_{adv}(D(t_{i+step})) &= \frac{1}{2} \mathbb{E}_{HSR(t_{i+step})_{real} \sim p(t_{i+step})} [(\delta(t_{i+step})_{real} - 1)^2] \\ &+ \frac{1}{2} \mathbb{E}_{HSR(t_i)_{real} \sim p(t_i)} [(\delta(t_{i+step})_{fake})^2], \end{aligned} \quad (12)$$

$$\begin{aligned} \mathcal{L}_{adv}(G_f) &= \frac{1}{2} \mathbb{E}_{HSR(t_i)_{real} \sim p(t_i)} [(\delta(t_{i+step})_{fake} - 1)^2], \end{aligned} \quad (13)$$

$$\begin{aligned} \mathcal{L}_{adv}(D(t_i)) &= \frac{1}{2} \mathbb{E}_{HSR(t_i)_{real} \sim p(t_i)} [(\delta(t_i)_{real} - 1)^2] \\ &+ \frac{1}{2} \mathbb{E}_{HSR(t_{i+step})_{real} \sim p(t_{i+step})} [(\delta(t_i)_{fake})^2], \end{aligned} \quad (14)$$

$$\begin{aligned} \mathcal{L}_{adv}(G_b) &= \frac{1}{2} \mathbb{E}_{HSR(t_{i+step})_{real} \sim p(t_{i+step})} [(\delta(t_i)_{fake} - 1)^2], \end{aligned} \quad (15)$$

where  $p(t_{i+step})$  and  $p(t_i)$  indicate to the distributions of  $HSR(t_{i+step})_{real}$  and  $HSR(t_i)_{real}$ , respectively.

In our preliminary experiments, training using the adversarial losses of regular GANs was not successful. Also, training using WGAN-GP required more time. So the adversarial losses of LSGANs were finally chosen.

#### 3.1.2 Cycle-Consistency Loss

We apply the cycle-consistency loss into the time-series domain to create temporal causality [58]. In other words, the

cycle-consistency loss is used to satisfy the following conditions:

$$HSR(t_{i+step})_{cycled} \approx HSR(t_{i+step})_{real}, \quad (16)$$

$$HSR(t_i)_{cycled} \approx HSR(t_i)_{real}. \quad (17)$$

Therefore, the cycle-consistency loss, represented in purple in Figure 1, is as follows:

$$\begin{aligned} \mathcal{L}_{cyc}(G_f, G_b) &= \mathbb{E}_{HSR(t_{i+step})_{real} \sim p(t_{i+step})} [L1(t_{i+step})_{cycled}] \\ &+ \mathbb{E}_{HSR(t_i)_{real} \sim p(t_i)} [L1(t_i)_{cycled}]. \end{aligned} \quad (18)$$

Here,  $p(t_{i+step})$  and  $p(t_i)$  indicate to the distributions of  $HSR(t_{i+step})_{real}$  and  $HSR(t_i)_{real}$ , respectively.

#### 3.1.3 Pixel Loss

We apply pixel losses with adversarial losses to satisfy the following conditions:

$$HSR(t_{i+step})_{real} \approx HSR(t_{i+step})_{fake}, \quad (19)$$

$$HSR(t_i)_{real} \approx HSR(t_i)_{fake}. \quad (20)$$

To satisfy Equations (19) and (20), the pixel loss (forward)  $\mathcal{L}_{pix}(G_f)$  and pixel loss (backward)  $\mathcal{L}_{pix}(G_b)$  are as follows:

$$\begin{aligned} \mathcal{L}_{pix}(G_f) &= \mathbb{E}_{HSR_i \sim (p(t_i), p(t_{i+step}))} [L1(t_{i+step})_{fake}], \end{aligned} \quad (21)$$

$$\begin{aligned} \mathcal{L}_{pix}(G_b) &= \mathbb{E}_{HSR_i \sim (p(t_i), p(t_{i+step}))} [L1(t_i)_{fake}], \end{aligned} \quad (22)$$

where  $p(t_i)$  and  $p(t_{i+step})$  indicate to the distributions of  $HSR(t_i)_{real}$  and  $HSR(t_{i+step})_{real}$ , respectively. Also, in Figure 1,  $\mathcal{L}_{pix}(G_f)$  and  $\mathcal{L}_{pix}(G_b)$  are represented in blue and red, respectively.

In our preliminary experiments, using only adversarial losses and cycle-consistency loss did not capture the changes over time well. However, the identity loss, additionally adopted in the original CycleGAN to improve performance [58], could not be used in our experiments because it breaks temporal causality. For example,  $G_f$  should always be a mapping from the present to the future, but if the identity loss is added, it can also represent a mapping from the present to the present. Instead of the identity loss, we added pixel losses, inspired by Pix2Pix [22], to help  $G_f$  and  $G_b$  capture the temporal changes.

### 3.1.4 Total Objective Function

According to Equations (12)–(15), (18), (21), and (22), total objective functions are as follows:

$$\begin{aligned} \min_{D(t_{i+step})} : \mathcal{L}(D(t_{i+step})) \\ = \mathcal{L}_{adv}(D(t_{i+step})), \end{aligned} \quad (23)$$

$$\begin{aligned} \min_{G_f} : \mathcal{L}(G_f) \\ = \mathcal{L}_{adv}(G_f) \\ + \lambda_{cyc} \mathcal{L}_{cyc}(G_f, G_b) + \lambda_{pix} \mathcal{L}_{pix}(G_f), \end{aligned} \quad (24)$$

$$\begin{aligned} \min_{D(t_i)} : \mathcal{L}(D(t_i)) \\ = \mathcal{L}_{adv}(D(t_i)), \end{aligned} \quad (25)$$

$$\begin{aligned} \min_{G_b} : \mathcal{L}(G_b) \\ = \mathcal{L}_{adv}(G_b) \\ + \lambda_{cyc} \mathcal{L}_{cyc}(G_f, G_b) + \lambda_{pix} \mathcal{L}_{pix}(G_b), \end{aligned} \quad (26)$$

where  $\lambda_{cyc} \in \mathbb{R}^+$  and  $\lambda_{pix} \in \mathbb{R}^+$  control their relative importance. Our objective functions satisfy Equations (16), (17), (19), and (20); thus, our model achieves the following final goals:

$$\begin{aligned} HSR(t_{i+step})_{real} &\approx HSR(t_{i+step})_{fake} \\ &\approx HSR(t_{i+step})_{cycled}, \end{aligned} \quad (27)$$

$$\begin{aligned} HSR(t_i)_{real} &\approx HSR(t_i)_{fake} \\ &\approx HSR(t_i)_{cycled}. \end{aligned} \quad (28)$$

These goals guarantee the temporal causality of *Cycle 1* and *Cycle 2*.

Since our experiments are focused on regional precipitation nowcasting with relatively little dynamic changes compared to wide-range precipitation nowcasting, even simple objective functions (23)–(26) make successful results. However, more precise objective functions will be needed to accommodate a huge scale of spatial changes in precipitation.

## 3.2. Network Architecture

Our generators  $G_f$  and  $G_b$  have the same network architectures. And our discriminators  $D(t_{i+step})$  and  $D(t_i)$  have the same network architectures. The network architectures of our discriminators and generators are shown in Figure 2.

### 3.2.1 Generator Architecture

The generator network has an encoder, 16 squeeze-and-excitation (SE)-residual blocks [19, 20], and a decoder. The encoder reduces the size of the input HSR and extracts 256

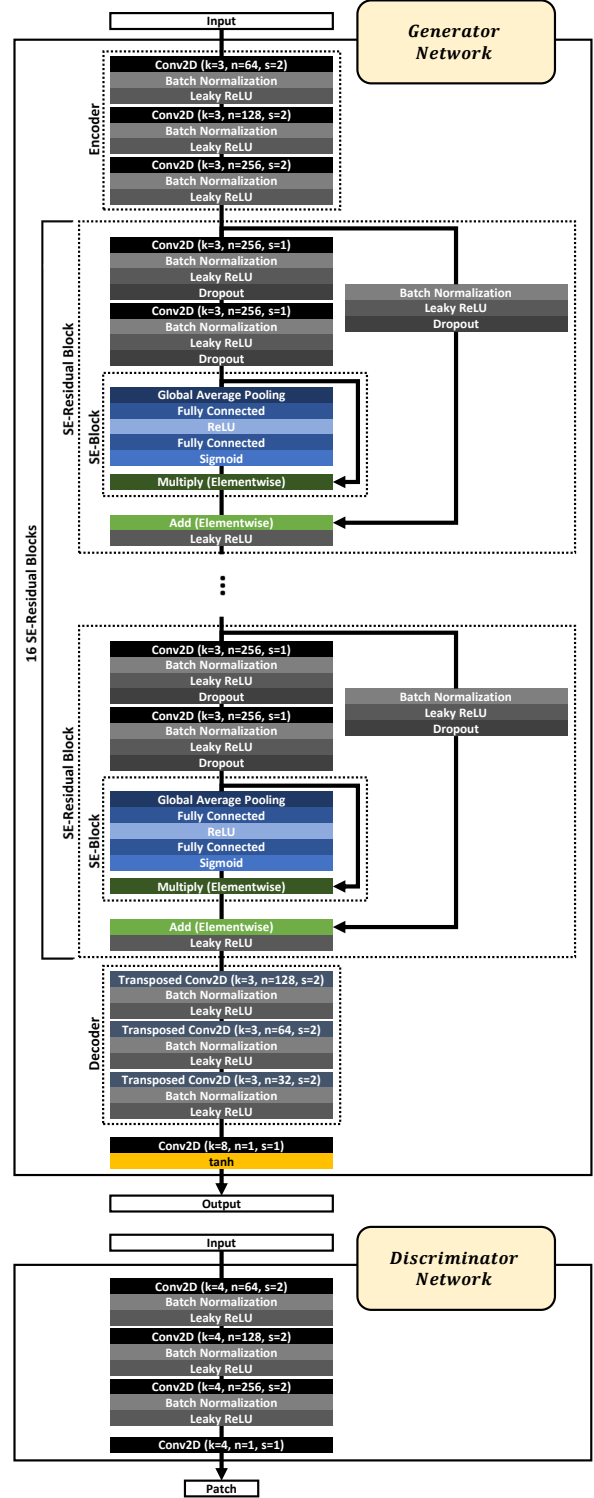


Figure 2. Network architectures of generators and discriminators. The generators consist of the encoder, squeeze-and-excitation (SE)-residual blocks [19, 20], and decoder. The discriminators use the architecture of PatchGANs [30]. Here,  $k$ ,  $n$ , and  $s$  in the convolution layers and the transposed convolution layers are the kernel size, the number of feature maps, and the stride, respectively.



features. The SE-residual block is a core part of the generator network, a combination of the residual block and the SE-block. We add the dropout layers in the residual blocks for robustness. We use a small number of residual blocks, so we do not use the bottleneck block according to the design policy of the original ResNet. The decoder is paired with the encoder and restores the size of the reduced HSR data. The convolution layer just before the output is for fine resizing, and tanh is used for the final activation function.

In our preliminary experiments, U-Net architecture [46], which is widely used in the meteorological field, failed to learn as the data distributions became more diverse. We estimated that the failure of U-Net is due to the skip-connection techniques using the concatenation layers that copy and paste channels. Instead, we used the residual blocks which use elementwise sum operations for skip-connection techniques [19]. Also, the addition of the SE-blocks increased the quality of the generated HSR data [20].

### 3.2.2 Discriminator Architecture

The discriminator network uses the architecture of Patch-GANs [30]. In other words, our discriminator network classifies whether the output data patch is real or fake. Such the patch-unit discriminator is lighter than the full-data discriminator [22]. We use the  $31 \times 31$  patch size to distinguish. However, the patch size can be flexibly changed according to the size of the input data.

## 4. Results

We first describe our precipitation dataset and training details. We then compare the proposed method with two precipitation nowcasting methods used in actual weather radar operational systems. Finally, we discuss the limitations of the proposed model.

### 4.1. Dataset

The radar reflectivity data, the source of our precipitation dataset, are collected from the weather radars installed throughout Korea. The collected reflectivity data are regenerated as composite HSR data with reflectivity-rainfall rate equation and the quality control process [41]. The spatial resolution of the composite HSR data is 1km, and the temporal resolution is 5 minutes. From a spatial point of view, we extract  $240\text{km} \times 240\text{km}$  in the central region of Korea including Seoul from the composite HSR data. From a temporal point of view, we extract the composite HSR data for six months from July to December 2021. The extracted HSR data form the pair as in Equation (1). The default of *step*, the interval between paired data, is 2. In other words, the default time interval between paired data is 10 minutes.

### 4.2. Training Details

In the data preprocessing process, we remove the pair  $HSR_i$ , where  $HSR(t_i)_{real} == HSR(t_{i+step})_{real}$ . This is to focus on the extinction and development of radar echoes. Then, the refined dataset is normalized to  $[-1, 1]$ . In the generator and discriminator networks, we set the momentum for the moving average of batch normalization to 0.8 and the negative slope of Leaky ReLU to 0.2. We also set the drop rate of the dropout layer to 0.4. As the optimizer, we use the Adam with momentum parameters  $\beta_1 = 0.5$  and  $\beta_2 = 0.999$  [25]. The learning rate and batch size are set to 0.0002 and 16, respectively. In our objective functions (24) and (26), we set  $\lambda_{cyc} = 10$  and  $\lambda_{pix} = 10$ . We use the NVIDIA A100 Tensor Core GPU for training.

### 4.3. Evaluation

We compare our method against two baselines both qualitatively and quantitatively. The first baseline is MAPLE [54], a QPF model. The second baseline is ConvLSTM based on RNNs [48]. Both baselines are currently used in weather radar operational systems and are methods that have been sufficiently verified in the real world. We do not consider the latest nowcasting method without officially published source code and parameter values by the original author as a baseline for comparison. For qualitative evaluation, we use the CSI as a metric [47]. For quantitative evaluation, we use PSNR and SSIM as metrics [55]. CSI, PSNR, and SSIM are all better high.

As shown in Figure 3, in the experimental results of the CSI-based qualitative evaluation, our method guaranteed the highest score in all time points. The CSI of the proposed method remained relatively uniform compared to the CSI of the two baselines during a lead time of two hours. In particular, our model predicted the extinction of radar echoes better than MAPLE and details of radar echoes better than ConvLSTM.

As shown in Table 1, our proposed method scored the best in both PSNR and SSIM except for the first 10 minutes of prediction. The proposed method was also demonstrated to be superior to both baselines in the quantitative evaluation of predicted image quality.

### 4.4. Limitations

Since our proposed method does single-shot-to-single-shot prediction, it does iterative multi-step prediction in which it does one-step re-prediction in the predicted future. Therefore, one wrong prediction can lead to persistent prediction errors. The failure cases can be seen in Figure 4. Because precipitation nowcasting ultimately leads to weather forecasting, it is also sensitive to small radar echoes. It is an aspect that cannot be solved by qualitative or quantitative evaluation alone. A supervisor algorithm or a more sophisticated loss function will be required.

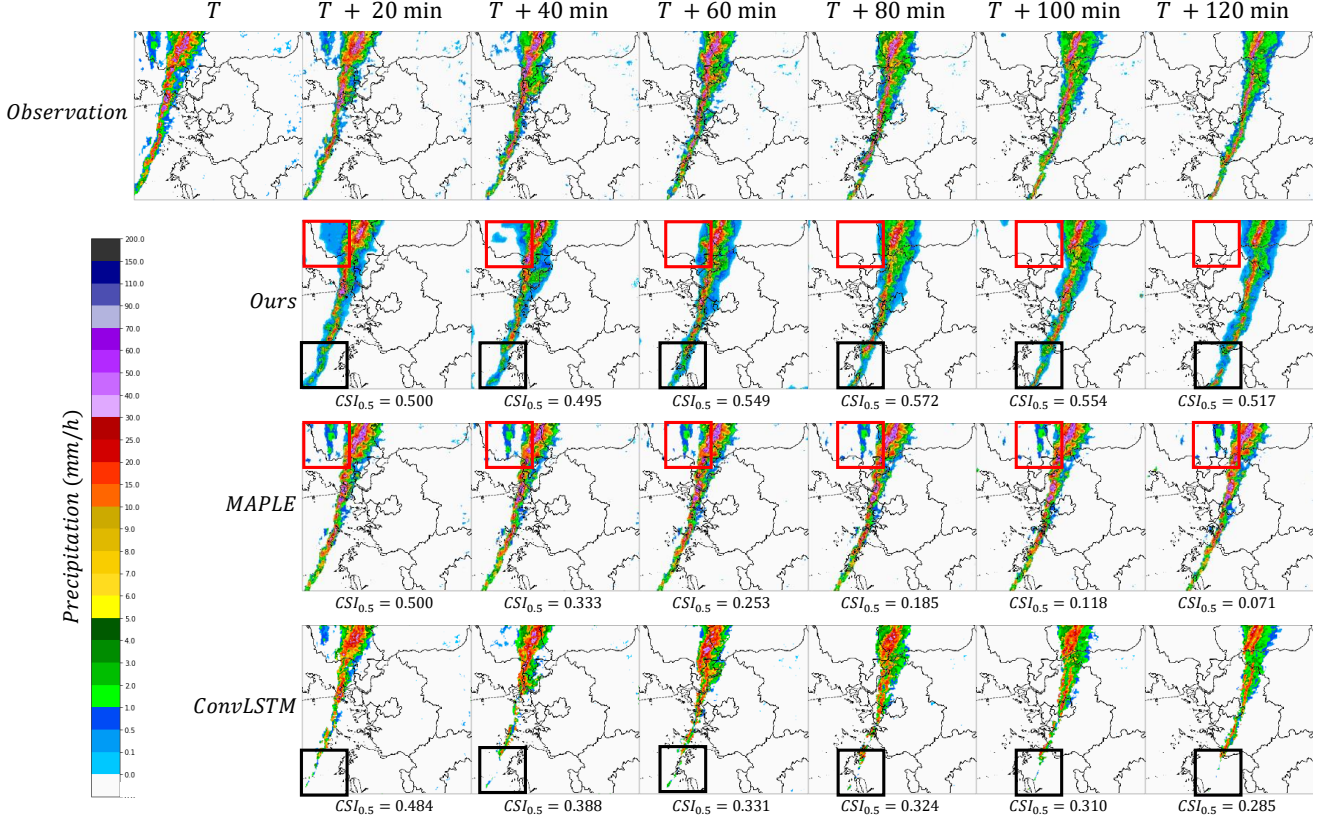


Figure 3. Qualitative comparisons of nowcasting using 3 different methods. The starting point  $T$  is 2022-09-23 01:00 (UTC). *Ours*, *MAPLE*, and *ConvLSTM* represent the proposed method, McGill algorithm for precipitation nowcasting by lagrangian extrapolation [54], and convolutional long short-term memory [48], respectively. The threshold of the critical success index (CSI) is 0.5mm/h. Our proposed method outperforms the others in the CSI-based evaluation. The red boxes show that our method predicts the extinction of radar echoes better than *MAPLE*. The black boxes show that our method predicts the shape of the squall line better than *ConvLSTM* [59].

Table 1. Quantitative comparisons of nowcasting using *MAPLE*, *ConvLSTM*, and our proposed method.

Method	Metric	+10min	+20min	+30min	+40min	+50min	+60min	+70min	+80min	+90min	+100min	+110min	+120min
Ours	PSNR	25.875	<b>25.558</b>	<b>24.689</b>	<b>24.641</b>	<b>24.532</b>	<b>24.462</b>	<b>24.428</b>	<b>24.192</b>	<b>24.181</b>	<b>24.125</b>	<b>24.109</b>	<b>24.104</b>
	SSIM	0.895	<b>0.898</b>	<b>0.887</b>	<b>0.885</b>	<b>0.872</b>	<b>0.870</b>	<b>0.859</b>	<b>0.854</b>	<b>0.849</b>	<b>0.844</b>	<b>0.843</b>	<b>0.842</b>
MAPLE	PSNR	<b>26.395</b>	25.050	24.037	23.517	23.288	23.351	23.428	23.057	23.091	23.981	23.467	23.818
	SSIM	<b>0.915</b>	0.897	0.878	0.864	0.854	0.847	0.841	0.837	0.833	0.830	0.834	0.836
ConvLSTM	PSNR	22.985	22.599	21.132	20.825	20.463	20.098	20.299	20.542	19.997	20.223	20.496	19.593
	SSIM	0.861	0.858	0.853	0.850	0.845	0.843	0.842	0.841	0.833	0.829	0.829	0.821

## 5. Conclusion

We proposed a precipitation nowcasting method by extending the CycleGAN into the time domain. We gave up the identity loss of the existing CycleGAN and added a pixel loss for temporal causality. Two generators and two discriminators were trained in the complementary cycles. One of the generators learned temporal mapping toward the future and the other learned temporal mapping toward the past. We also proposed a network architectures using SE-residual blocks for robust nowcasting. For both qualitative and quantitative evaluation, our proposed method outper-

formed the representative actual precipitation nowcasting methods.

## Acknowledgments

We special thank Young-A Oh for many valuable comments. This research was supported by the “Development of radar based severe weather nowcasting technology (KMA2021-03122)” of “Development of radar application technology supporting weather forecast” project funded by the Weather Radar Center, Korea Meteorological Administration.





- part i: Description of the methodology. *Monthly Weather Review*, 130(12):2859–2873, 2002. 2
- [14] U. Germann and I. Zawadzki. Scale dependence of the predictability of precipitation from continental radar images. part ii: Probability forecasts. *Journal of Applied Meteorology and Climatology*, 43(1):74–89, 2004. 2
- [15] I. Goodfellow, J. Pouget-Abadie, M. Mirza, B. Xu, D. Warde-Farley, S. Ozair, A. Courville, and Y. Bengio. Generative adversarial nets. In *NeurIPS*, 2014. 1, 2
- [16] I. Goodfellow, J. Pouget-Abadie, M. Mirza, B. Xu, D. Warde-Farley, S. Ozair, A. Courville, and Y. Bengio. Generative adversarial networks. *Communications of the ACM*, 63(11):139–144, 2020. 1, 2
- [17] I. Gulrajani, F. Ahmed, M. Arjovsky, V. Dumoulin, and A. Courville. Improved training of wasserstein gans. In *NeurIPS*, 2017. 2
- [18] L. Han, H. Liang, H. Chen, W. Zhang, and Y. Ge. Convective precipitation nowcasting using u-net model. *IEEE Transactions on Geoscience and Remote Sensing*, 60:1–8, 2022. 2
- [19] K. He, X. Zhang, S. Ren, and J. Sun. Deep residual learning for image recognition. In *CVPR*, 2016. 2, 5, 6
- [20] J. Hu, L. Shen, and G. Sun. Squeeze-and-excitation networks. In *CVPR*, 2018. 5, 6, 13
- [21] X. Huang, M-Y. Liu, S. Belongie, and J. Kautz. Multimodal unsupervised image-to-image translation. In *ECCV*, 2018. 2
- [22] P. Isola, J-Y. Zhu, T. Zhou, and A. A. Efros. Image-to-image translation with conditional adversarial networks. In *CVPR*, 2017. 2, 4, 6
- [23] Z. Jiang, R. Zhang, Y. Guo, M. Hu, L. He, F. Li, and Z. Zhu. Noise interference reduction in vision module of intelligent plant cultivation robot using better cycle gan. *IEEE Sensors Journal*, 22(11):11045–11055, 2022. 2
- [24] D. M. Jose, A. M. Vincent, and G. S. Dwarakish. Improving multiple model ensemble predictions of daily precipitation and temperature through machine learning techniques. *Scientific Reports*, 12(4678):1–25, 2022. 2
- [25] D. P. Kingma and J. Ba. Adam: A method for stochastic optimization. In *ICLR*, 2015. 6
- [26] M. Ko, E. Cha, S. Suh, H. Lee, J-J. Han, J. Shin, and B. Han. Self-supervised dense consistency regularization for image-to-image translation. In *CVPR*, 2022. 2
- [27] Y-H. Kwon and M-G. Park. Predicting future frames using retrospective cycle gan. In *CVPR*, 2019. 2
- [28] C-K. Lee, Y-J. Cheon, and W-Y. Hwang. Least squares generative adversarial networks-based anomaly detection. *IEEE Access*, 10:26920–26930, 2022. 2
- [29] D. I. Lee, Y. Hwang, Y. Kim, and C. H. You. Application of high spatial and temporal resolution nowcasting in Korea. In *AMS*, 2017. 2
- [30] C. Li and M. Wand. Precomputed real-time texture synthesis with markovian generative adversarial networks. In *ECCV*, 2016. 5, 6
- [31] W. Li and J. Wang. Residual learning of cycle-gan for seismic data denoising. *IEEE Access*, 9:11585–11597, 2021. 2
- [32] Y. Li, Z. Gan, Y. Shen, J. Liu, Y. Cheng, Y. Wu, L. Carin, D. Carlson, and J. Gao. Storygan: A sequential conditional gan for story visualization. In *CVPR*, 2019. 2
- [33] M-Y. Liu, T. Breuel, and J. Kautz. Unsupervised image-to-image translation networks. In *NeurIPS*, 2017. 2
- [34] M-Y. Liu and O. Tuzel. Coupled generative adversarial networks. In *NeurIPS*, 2016. 2
- [35] C. Luo, X. Li, and Y. Ye. Pfst-lstm: A spatiotemporal lstm model with pseudoflow prediction for precipitation nowcasting. *IEEE Journal of Selected Topics in Applied Earth Observations and Remote Sensing*, 14:843–857, 2021. 2
- [36] X. Mao, Q. Li, H. Xie, R. Y. K. Lau, Z. Wang, and S. P. Smolley. Least squares generative adversarial networks. In *ICCV*, 2017. 2, 4
- [37] X. Mao, Q. Li, H. Xie, R. Y. K. Lau, Z. Wang, and S. P. Smolley. On the effectiveness of least squares generative adversarial networks. *IEEE TPAMI*, 41(12):2947–2960, 2019. 2, 4
- [38] S. Mathew, S. Nadeem, S. Kumari, and A. Kaufman. Augmenting colonoscopy using extended and directional cycle-gan for lossy image translation. In *CVPR*, 2020. 2
- [39] S. Metta, J. V. Hardenberg, L. Ferraris, N. Rebora, and A. Provenzale. Precipitation nowcasting by a spectral-based nonlinear stochastic model. *Journal of Hydrometeorology*, 10(5):1285–1297, 2009. 2
- [40] D. Mukherjee, P. Saha, D. Kaplun, A. Sinitca, and R. Sarkar. Brain tumor image generation using an aggregation of gan models with style transfer. *Scientific Reports*, 12(9141):1–16, 2022. 2
- [41] Y-A. Oh, H-L. Kim, and M-K. Suk. Clutter elimination algorithm for non-precipitation echo of radar data considering meteorological and observational properties in polarimetric measurements. *Remote Sensing*, 12(22):3790, 2020. 6, 11
- [42] Y-A. Oh, M-K. Suk, S-H. Jung, and K-I. Jang. Hybrid surface rainfall estimation for operational application using dual polarization radar network in Korea. In *ERAD*, 2018. 2, 11
- [43] T. Park, A. A. Efros, R. Zhang, and J-Y. Zhu. Contrastive learning for unpaired image-to-image translation. In *ECCV*, 2020. 2
- [44] C. E. Pierce, E. Ebert, A. W. Seed, M. Sleight, C. G. Collier, N. I. Fox, N. Donaldson, J. W. Wilson, R. Roberts, and C. K. Mueller. The nowcasting of precipitation during sydney 2000: an appraisal of the qpf algorithms. *Weather and Forecasting*, 19(1):7–21, 2004. 2
- [45] S. Ravuri, K. Lenc, M. Willson, D. Kangin, R. Lam, P. Mirowski, M. Fitzsimons, M. Athanassiadou, S. Kashem, S. Madge, R. Prudden, A. Mandhane, A. Clark, A. Brock, K. Simonyan, R. Hadsell, N. Robinson, E. Clancy, A. Arribas, and S. Mohamed. Skilful precipitation nowcasting using deep generative models of radar. *Nature*, 597(7878):672–677, 2021. 2
- [46] O. Ronneberger, P. Fischer, and T. Brox. U-net: Convolutional networks for biomedical image segmentation. In *MICCAI*, 2015. 2, 6
- [47] J. T. Schaefer. The critical success index as an indicator of warning skill. *Weather and Forecasting*, 5(4):570–575, 1990. 1, 6, 12
- [48] X. Shi, Z. Chen, H. Wang, D. Yeung, W. Wong, and W. Woo. Convolutional lstm network: A machine learning approach for precipitation nowcasting. In *NeurIPS*, 2015. 1, 2, 6, 7, 11

- [49] X. Shi, Z. Gao, L. Lausen, H. Wang, D-Y. Yeung, W-K. Wong, and W-C. Woo. Deep learning for precipitation nowcasting: A benchmark and a new model. In *NeurIPS*, 2017. [2](#)
- [50] C. J. Short and J. Petch. Reducing the spin-up of a regional nwp system without data assimilation. *Quarterly Journal of the Royal Meteorological Society*, 148(745):1623–1643, 2022. [1](#)
- [51] M. Siam, S. Valipour, M. Jagersand, and N. Ray. Convolutional gated recurrent networks for video segmentation. In *ICIP*, 2017. [2](#)
- [52] J. Sun, M. Xue, J. W. Wilson, I. Zawadzki, S. P. Ballard, J. Onvlee-Hooimeyer, P. Joe, D. M. Barker, P-W. Li, B. Golding, M. Xu, and J. Pinto. Use of nwp for nowcasting convective precipitation: Recent progress and challenges. *Bulletin of the American Meteorological Society*, 95(3):409–426, 2014. [1](#), [2](#)
- [53] K. Trebing, T. Stańczyk, and S. Mehrkanoon. Smaat-unet: Precipitation nowcasting using a small attention-unet architecture. *Pattern Recognition Letters*, 145:178–186, 2021. [2](#)
- [54] B. J. Turner, I. Zawadzki, and U. Germann. Predictability of precipitation from continental radar images. part iii: Operational nowcasting implementation (maple). *Journal of Applied Meteorology and Climatology*, 43(2):231–248, 2004. [1](#), [2](#), [6](#), [7](#), [11](#)
- [55] Z. Wang, A. C. Bovik, H. R. Sheikh, and E. P. Simoncelli. Image quality assessment: from error visibility to structural similarity. *IEEE TIP*, 13(4):600–612, 2004. [2](#), [6](#), [12](#)
- [56] J. W. Wilson, N. A. Crook, C. K. Mueller, J. Sun, and M. Dixon. Nowcasting thunderstorms: A status report. *Bulletin of the American Meteorological Society*, 79(10):2079–2100, 1998. [1](#)
- [57] L. Zhang, X. Chen, X. Tu, P. Wan, N. Xu, and K. Ma. Wavelet knowledge distillation: Towards efficient image-to-image translation. In *CVPR*, 2022. [2](#)
- [58] J-Y. Zhu, T. Park, P. Isola, and A. A. Efros. Unpaired image-to-image translation using cycle-consistent adversarial networks. In *ICCV*, 2017. [1](#), [2](#), [4](#)
- [59] E. J. Zipser. Mesoscale and convective-scale downdrafts as distinct components of squall-line structure. *Monthly Weather Review*, 105(12):1568–1589, 1977. [7](#)
- [60] Z. Zou, W. Li, T. Shi, Z. Shi, and J. Ye. Generative adversarial training for weakly supervised cloud matting. In *ICCV*, 2019. [2](#)

# Regional Precipitation Nowcasting Based on CycleGAN Extension

## Supplementary Material

Jaeho Choi, Yura Kim, Kwang-Ho Kim, Sung-Hwa Jung, and Ikhyun Cho  
Weather Radar Center, Korea Meteorological Administration

{jaehochoi2021, yrkim110, khkim777, shjung95}@korea.kr, ehcho@kma.go.kr

### Overview

This supplementary material is structured as follows.

- Appendix A briefly describes the creation process of hybrid surface rainfall (HSR) data used in our experiments.
- Appendix B provides additional experimental results in the Jeju Island area.
- Appendix C provides an ablation study about the architecture of generators.

### A. Creation Process of Hybrid Surface Rainfall (HSR)

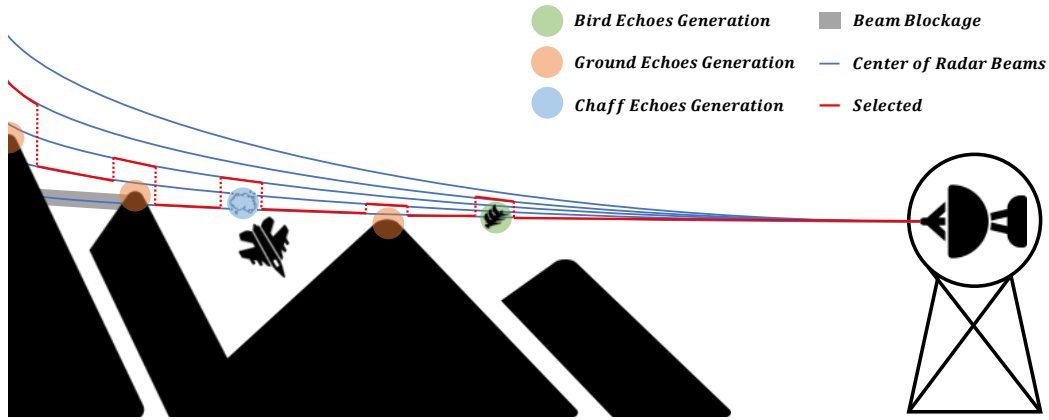


Figure 1. Beam selection strategy for hybrid surface rainfall (HSR) data construction.

As shown in Figure 1, the hybrid surface rainfall (HSR) data select the reflectivity of the beam that is closest to the ground at each horizontal distance from weather radar and is less affected by non-meteorological echoes and beam blockages [41,42]. Here, the non-meteorological echoes include bird echoes, ground echoes, chaff echoes, *etc.*, which are the major obstacles to precipitation estimation. The collected reflectivity data are converted into HSR data via the reflectivity-rainfall equation considering regional characteristics. HSR data are currently being used for weather forecasts in Korea.

### B. Additional Results: A Case in Jeju Island

Figure 2 shows the results of precipitation nowcasting in Jeju Island during the lead time of two hours from 2022-09-11 17:30 (UTC). *Ours* represents our proposed method. *MAPLE* represents the McGill algorithm for precipitation nowcasting by lagrangian extrapolation [54]. And *ConvLSTM* represents the convolutional long short-term memory [48]. Our proposed method provides more accurate prediction results than *MAPLE* and *ConvLSTM*.

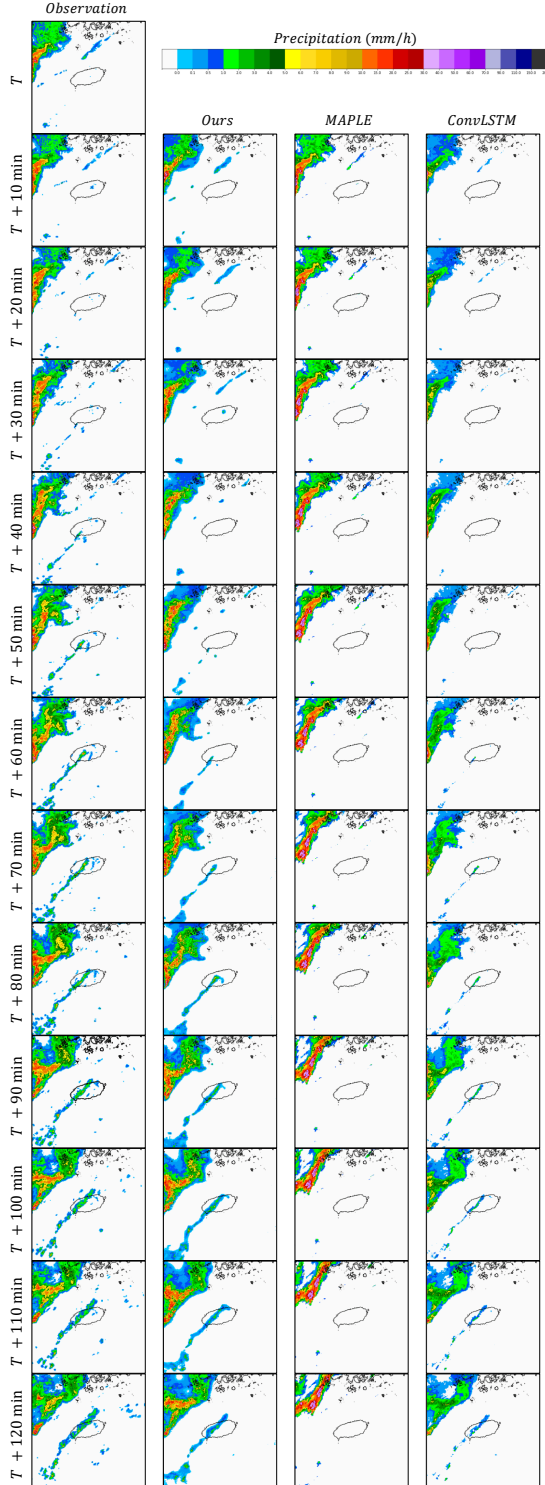


Figure 2. Comparisons of precipitation nowcasting in the Jeju Island area using 3 different methods. The starting point  $T$  is 2022-09-11 17:30 (UTC).

Table 1. Qualitative and quantitative evaluation scores of Figure 2.

Time	Metric	Ours	MAPLE	ConvLSTM
$T + 10min$	CSI <sub>0.5</sub>	<b>0.788</b>	0.780	0.607
	CSI <sub>2.0</sub>	0.468	<b>0.472</b>	0.409
	PSNR	32.031	31.704	<b>33.280</b>
	SSIM	0.956	0.963	<b>0.965</b>
$T + 20min$	CSI <sub>0.5</sub>	<b>0.774</b>	0.772	0.545
	CSI <sub>2.0</sub>	<b>0.565</b>	0.531	0.538
	PSNR	31.389	30.528	<b>33.244</b>
	SSIM	0.956	0.961	<b>0.965</b>
$T + 30min$	CSI <sub>0.5</sub>	0.742	<b>0.780</b>	0.496
	CSI <sub>2.0</sub>	<b>0.636</b>	0.565	0.555
	PSNR	<b>32.219</b>	28.773	29.786
	SSIM	<b>0.956</b>	0.955	0.951
$T + 40min$	CSI <sub>0.5</sub>	0.700	<b>0.709</b>	0.490
	CSI <sub>2.0</sub>	<b>0.638</b>	0.561	0.588
	PSNR	<b>32.121</b>	27.431	31.697
	SSIM	<b>0.949</b>	0.942	0.943
$T + 50min$	CSI <sub>0.5</sub>	<b>0.657</b>	0.589	0.495
	CSI <sub>2.0</sub>	<b>0.632</b>	0.525	0.560
	PSNR	<b>30.047</b>	26.713	30.024
	SSIM	<b>0.931</b>	0.923	0.930
$T + 60min$	CSI <sub>0.5</sub>	<b>0.646</b>	0.545	0.558
	CSI <sub>2.0</sub>	<b>0.593</b>	0.457	0.466
	PSNR	<b>32.268</b>	26.266	31.442
	SSIM	<b>0.930</b>	0.905	0.922
$T + 70min$	CSI <sub>0.5</sub>	<b>0.665</b>	0.487	0.612
	CSI <sub>2.0</sub>	<b>0.560</b>	0.390	0.399
	PSNR	29.755	25.818	<b>30.910</b>
	SSIM	<b>0.919</b>	0.888	0.913
$T + 80min$	CSI <sub>0.5</sub>	<b>0.659</b>	0.435	0.612
	CSI <sub>2.0</sub>	<b>0.558</b>	0.346	0.385
	PSNR	28.776	25.467	<b>29.935</b>
	SSIM	0.903	0.876	<b>0.912</b>
$T + 90min$	CSI <sub>0.5</sub>	<b>0.658</b>	0.414	0.614
	CSI <sub>2.0</sub>	<b>0.554</b>	0.315	0.401
	PSNR	28.764	25.170	<b>28.832</b>
	SSIM	<b>0.903</b>	0.869	0.901
$T + 100min$	CSI <sub>0.5</sub>	<b>0.659</b>	0.399	0.642
	CSI <sub>2.0</sub>	<b>0.566</b>	0.293	0.429
	PSNR	<b>28.748</b>	24.922	27.775
	SSIM	<b>0.899</b>	0.864	0.886
$T + 110min$	CSI <sub>0.5</sub>	<b>0.636</b>	0.369	0.621
	CSI <sub>2.0</sub>	<b>0.544</b>	0.248	0.400
	PSNR	<b>27.725</b>	24.905	26.779
	SSIM	<b>0.897</b>	0.864	0.885
$T + 120min$	CSI <sub>0.5</sub>	<b>0.605</b>	0.348	0.581
	CSI <sub>2.0</sub>	<b>0.535</b>	0.221	0.384
	PSNR	<b>27.768</b>	24.944	26.747
	SSIM	<b>0.900</b>	0.866	0.884

As shown in Table 1, we use the critical success index (CSI) as a qualitative metric and the peak signal-to-noise ratio (PSNR) and structural similarity index measure (SSIM) as quantitative metrics [47, 55]. In particular, CSI at thresholds 0.5mm/h and 2.0mm/h are represented as CSI<sub>0.5</sub> and CSI<sub>2.0</sub>, respectively. Overall, all evaluation scores have a decreasing trend with time, and our proposed method achieves the best score in the most time slots.

In a case study in Jeju Island, the spatial and temporal resolutions of the HSR dataset used for training are 1km and 10 minutes, respectively. From a spatial point of view, the training dataset covers 240km × 240km centered on Jeju Island. From a temporal point of view, the training dataset covers six months from July to December 2021.



### C. Ablation Study

We remove all squeeze-and-excitation (SE)-blocks from the architecture of generators [20], with no changes in other experimental conditions. We then check the influence of SE-blocks via comparison with before removal.

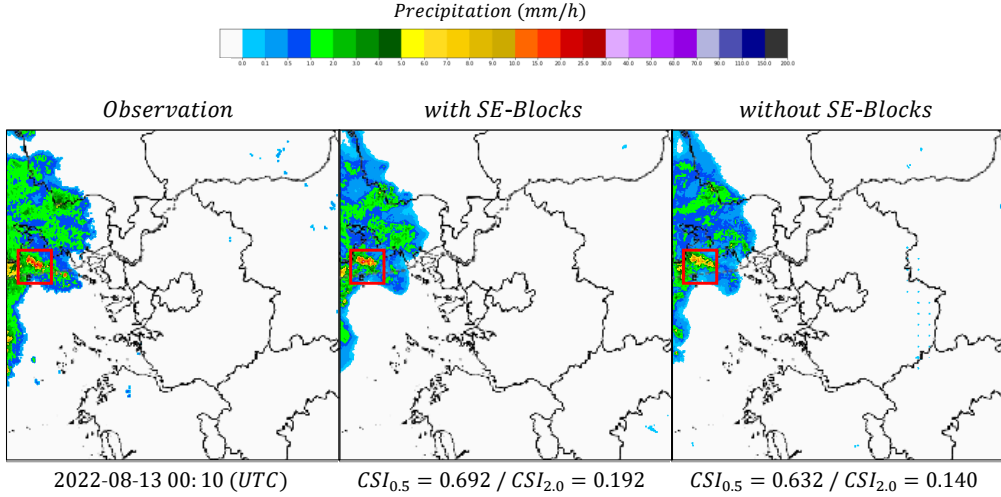


Figure 3. Qualitative comparisons with and without squeeze-and-excitation (SE)-blocks. The subscripts of CSI represent thresholds.

Table 2. Quantitative comparisons with and without SE-blocks.

Metric	with SE-blocks	without SE-blocks
PSNR	30.881	28.804
SSIM	0.893	0.880

As shown in Figure 3, higher-quality predicted HSR data could be generated in the presence of SE-blocks. In particular, the red boxes show that SE-blocks are more advantageous in capturing detailed echoes. The CSI scores are also better with the SE-blocks than without them.

Table 2 shows the average PSNR and SSIM scores for the two months of August to September 2022 of predicted HSR at a lead time of 10 minutes. We find that the use of SE-blocks is advantageous in both quantitative metrics. Therefore, it is appropriate to adopt the SE-blocks as parts of the generator architectures for our precipitation nowcasting.